On the Relation Between ROC and CMC

Raymond N. J. Veldhuis, *Senior Member, IEEE*, and Kiran Raja, *Senior Member, IEEE*

Abstract—We formulate a compact relation between the probabilistic Receiver Operating Characteristic (ROC) and the probabilistic Cumulative Match Characteristic (CMC) that predicts every entry of the probabilistic CMC as a functional on the probabilistic ROC. This result is shown to be valid for individual probabilistic ROCs and CMCs of single identities, based on the assumption that each identity has individual mated and nonmated Probabilitic Density Functions (PDF). Furthermore, it is shown that the relation still holds between the global probabilistic CMC of a gallery of identities and the average probabilistic ROC obtained by averaging the individual probabilistic ROCs of these identities involved over constant False Match Rates (FMR). We illustrate that the difference between individual probabilistic ROCs and the difference between global and average probabilistic ROCs provide an explanation for the discrepancies observed in the literature. The new formulation of the relation between probabilistic ROCs and CMCs allows us to prove that the probabilistic CMC plotted as a function of fractional rank, i.e., linearly compressed to a domain ranging from 0 to 1, will converge to the average probabilistic ROC when the gallery size increases. We illustrate our findings by experiments on synthetic and on face, fingerprint, and iris data.

Index Terms—Biometric verification, closed-set identification, ROC, CMC.

I. INTRODUCTION

BIOMETRIC recognition systems proposed in the literature are often evaluated in the application contexts of *biometric verification* or *biometric identification*. The goal of biometric verification is to verify an identity claim based on two samples of biometric data, e.g., fingerprints, facial images, or iris scans. One of these samples, the *reference*, is usually stored in advance in a database, called the *gallery*, during a process called enrolment. The other sample, produced by the identity at verification time, is called the *probe*. The identity claim is accepted if the two samples are sufficiently similar, otherwise it is rejected. The goal of biometric identification is to determine the identity of an individual by comparing a probe to all the identity-labeled references stored in the gallery. If the identity of the individual is known to be represented in the gallery, we speak of *closed-set identification*. Otherwise,

we speak of *open-set* identification and an additional verification step is needed to establish whether the found identity is indeed that of the individual.

Biometric verification and open-set identification are used in operational applications, respectively for example in biometric e-gates [1] and immigration search databases [2]. Closed-set identification is not considered of operational value, because in operational biometric applications it can usually not be guaranteed that the probe is represented in the gallery [3]. It remains, however, relevant, because it is often used in scientific publications to quantify the recognition performance of biometric solutions, see [4], [5], [6], [7] for some recent examples.

This paper presents new relations between the *Receiver Operating Characteristic* (ROC), characterising the performance of biometric verification, and the *Cumulative Match Characteristic* (CMC), characterising the performance of closed-set identification. This is theoretically relevant, because it extends the theory presented in [8], [9], [10] and sheds some light on discrepancies between theoretical and experimental results reported in [8], [9], [10], [11], [12], [13], [14].

A relation between the ROC and CMC is plausible to exist, because both biometric verification and identification share a *comparison* module that quantifies the similarity of two samples of biometric data by a *comparison score*. This can be a *similarity score*, increasing with similarity of the biometric samples, or a *dissimilarity score*, decreasing with similarity. Both are equivalent, therefore our discussions will be in terms of similarity scores only. The comparison function can be used as a biometric *comparator* by thresholding the similarity score. If it is above a predefined threshold, the comparator decides for a *match*, i.e., the biometric samples originate from the same individual. Otherwise, it decides for a *nonmatch*.

In biometric verification, the comparator's decision is used to accept an identity claim in case of a match. Otherwise it is rejected. In biometric closed-set identification, similarity scores are computed by comparing a probe with all the references in the gallery. The identity label of the entry that produces the highest similarity score is taken as the identity of the individual.

A similarity score obtained by comparing biometric samples from the same identity is called, in ISO terminology [15], a *mated* similarity score. A similarity score obtained by comparing samples from different identities is called a *nonmated* similarity score. A good verification or identification performance requires mated similarity scores to be higher than nonmated similarity scores. However, due to the inevitable variability of biometric data the ranges of mated and nonmated similarity scores are likely to overlap, which will lead to comparison errors. In particular, a *false match* occurs if a nonmated

Raymond N. J. Veldhuis is with the Faculty of EEMCS, University of Twente, 7500 AE Enschede, The Netherlands, and also with the Department of Information Security and Communication Technology, Norwegian University of Science and Technology, 2815 Gjøvik, Norway (e-mail: r.n.j.veldhuis@utwente.nl).

Kiran Raja is with the Department of Computer Science, Norwegian University of Science and Technology, 2815 Gjøvik, Norway.

similarity score is above the threshold and a *false nonmatch* occurs if a mated similarity score, is below the threshold. The corresponding error rates are the false-match rate (FMR), which is the fraction of false matches of all nonmated comparisons in a test, and the false-nonmatch rate (FNMR), which is the fraction of false nonmatches of all mated comparisons. The comparison threshold governs the trade-off between the FMR and the FNMR. Increasing it will result in a decreased FMR and an increased FNMR. In this paper it is more convenient to consider the *true-match rate* (TMR), which is fraction of correct matches obtained from all mated comparisons. It is the complement of the FNMR. The ROC plots the TMR as function of the FMR. The faster the ROC approaches 1 from the origin, the more discriminative the biometric comparison function is.

The typical error rates used in biometric verification are the *false-acceptance rate* (FAR) and the *false-rejection rate* (FRR). If failures to acquire can be ignored, a match decision will lead to acceptance of the identity claim. Then the FAR equals the FMR and the FRR equals the FNMR. Therefore, we will use FMR, FNMR, and ROC as performance characteristics for biometric verification. For a review of biometric testing terminology see [15] and [16].

The CMC is the commonly used performance indicator for biometric closet-set identification [8]. It is conveniently explained as follows. After comparison of a probe with all references in the gallery, the *r*-best candidate list is defined as the list of references with the *r* highest similarity scores. For a closed-set identification experiment the CMC shows, for *r* ranging from 1 to the gallery size, the fraction of mated comparisons that are in the *r*-best candidate list. The CMC for $r = 1$ is the *rank-1 recognition rate*, which is often presented as a scalar performance indicator for a biometric identification system. A disadvantage of the CMC, in comparison with the ROC, is that it depends on the gallery size. This makes it meaningless to compare CMCs and rank-1 recognition rates for different gallery sizes or to present them when the gallery size is not specified.

The ROC and the CMC as explained above are empirical measures, obtained through experiments on identity-labeled biometric datasets. Alternatively, we can set up a probabilistic model for biometric recognition performance by assuming that the similarity score is a realisation of a random variable drawn from one of two probability-density functions (PDFs), i.e., the mated PDF for mated similarity scores and the nonmated PDF for nonmated similarity scores. Such a probabilistic model is useful, because it can be used to analyse and predict properties of empirical quantities and of the relations between them. In a probabilistic model the empirical ROC and CMC are seen as estimates of the underlying probabilistic ROC and CMC.

As our main result in this article:

- We formulate a compact relation between the probabilistic ROC and the probabilistic CMC that, in our opinion, is more elegant than those presented earlier in [8], [9], [10]. It predicts every entry of the probabilistic CMC of a gallery of unique indentities as a functional on the probabilistic ROC (Refer Sections IV and V). This result is shown to be valid for individual probabilistic ROCs and

CMCs of single identities, based on the assumption that each identity has individual mated and nonmated PDFs.
- Furthermore, it is shown that the relation holds between the global probabilistic CMC of a gallery of unique identities and the average probabilistic ROC obtained by averaging the probabilistic ROCs of the identities in the gallery over constant FMRs (Sections V and IV). This average probabilistic ROC may differ from the global probabilistic ROC that is estimated in evaluation experiments and can be seen as the result of averaging individual ROCs over constant thresholds.
- We conclude that the difference between the average probabilistic ROC and the global ROC provides an explanation for the discrepancies observed in the literature (Section IV). The new formulation of the relation between probabilistic ROCs and CMCs allows us to prove that the probabilistic CMC plotted as a function of fractional rank, i.e., linearly compressed to a domain ranging from 0 to 1, will converge to the average probabilistic ROC when the gallery size increases.
- We illustrate our findings by experiments on real biometric data, namely the FRGC-V2 facial image dataset [17], the FVC2006 fingerprint dataset [18], and The Hong Kong Polytechnic University Cross-Spectral Iris Images Database [19]. Individual ROCs are hard to measure accurately in experiments because of the limited number of mated similarity scores that can generally be computed from a dataset. We, therefore, also include experiments on synthetic data that mimics real biometric data.

The remainder of this paper is organised as follows. Section II discusses previous work on the relation between ROC and CMC and the discrepancies that have been observed between theoretical results and experimental observations. Section III reviews biometric comparison, verification and identification from a probabilistic point of view. This section introduces the mathematical concepts that are needed for what follows. The main theoretical result of this paper on the relation between ROC and CMC is presented in Section IV. In particular, this section proves that the individual probabilistic CMC for a known identity can be computed as an integral transformation of the individual probabilistic ROC and that the global CMC can be computed in a similar way from an average ROC, with the average taken for fixed false-match probabilities. Section V uses the main result of Section IV to prove convergence properties of the probabilistic CMC including that with increasing size of the gallery the CMC converges in shape to an equidistantly sampled version of the probabilistic ROC. In Section VI the theoretical results are validated by experiments on synthetic and real biometric data. Finally, Section VII presents conclusions. For legibility, all proofs have been deferred to appendices.

II. RELATED WORK

In [8, Appendix A.5] the authors develop an expression to predict the CMC. It is stated in terms of the probability density functions for mated and nonmated similarity scores and does not immediately reveal the relation with the ROC.

They find that their prediction improves if score normalisation is applied prior to search. This is further analysed and confirmed in [20]. In [9] the authors extend the expression developed in [8] by including the probability that a mated similarity score is above a given threshold. Their result is explicitly based on the assumption that identities involved in the identification experiment set share the PDFs for mated and nonmated similarity scores, respectively. A relation of closed-set identification performance with the ROC is given in terms of the expected rank and the area under the ROC. This is rephrased in our Corollary 2. From their closed-set identification experiments, the authors conclude that the '[theoretical prediction] shows a prominent underestimation of the identification rate'.

In [10] the same prediction of the CMC as in [8] is presented, but without the restriction on the threshold. The assumption that all identities share the same PDFs or mated and nonmated similarity scores, respectively, is not explicitly made. A further approximation based on the assumption that PDF of the mated similarity scores is narrow compared with that of the nonmated similarity scores leads to a simpler expression. The authors illustrate that their theoretical predictions underestimate the empirical results through a set of experiments.

In [11], [12] it is concluded based on experimental data that it was needed to present both identification and verification performance when testing the performance of a biometric comparison system. This confirms that, although the relation between CMC and ROC such as presented in [8], [9], and [10] appears to be mathematically correct, it cannot be used to predict a CMC from a measured ROC. This is also confirmed by [13] in which examples from combinations of good experimental CMCs and poor ROCs were presented. In [14] it was found that splitting the data into 'goats', 'sheep', and 'lambs' according to Doddington's menagerie [21], resulted in distinct CMCs for each category, while they share the same ROC.

The findings reported in [8], [9], [10], [11], [12], [13], [14] are summarised well in [14] by the statement 'it is clear that support in the literature for a direct relationship between the ROC and CMC curves is mixed.' With this paper we hope to resolve the observed discrepancies between the CMC are predicted from the ROC and experimental results.

III. BIOMETRIC COMPARISON, VERIFICATION AND CLOSED-SET IDENTIFICATION

This section reviews biometric comparison from a probabilistic point of view. We assume that biometric data is random and hence similarity scores are random variables with distinct underlying PDFs for the mated and nonmated similarity scores. We also assume that these PDFs are individual. This will lead to the introduction of individual probabilistic ROCs and probabilistic CMCs. This is mainly of theoretical importance, as in most practical evaluations of biometric systems individual PDFs cannot be estimated reliably due to limited numbers of mated similarity scores. Therefore, the performance of biometric systems is commonly expressed in terms of the global, aggregated, ROCs and CMCs, and other performance indicators are derived from those. Moreover, global results are

better predictions of future performance, because future users are usually unknown.

Let the set χ denote a probe, and the set y a reference, either for verification or closed-set identification. We use a set notation to be as general as possible. For instance, χ and y may contain different numbers of biometric features or heterogeneous features such as from low- and high-resolution facial images. The only restriction we put on χ and y is that they allow for the computation of a similarity score $s = \mathrm{s}(\chi, y) \in \mathcal{S} \subset \mathbb{R}$, where $\mathcal{S}$ denotes the set of possible similarity score outcomes and $\mathbb{R}$ the set of real numbers. In our probabilistic approach, probe and reference are random. Hence, s is a random variable with a PDF depending on who produced χ and y. For χ and y produced by identities ω and ν, respectively, this PDF is denoted by $\phi(s|\omega, \nu)$.

Biometric performance characteristics are defined for a specific population $\mathcal{P}$ where probe identity ω and reference identity ν are drawn from. We define the mated similarity score PDF of an arbitrary probe identity $\omega \in \mathcal{P}$ by

$$\phi_{\mathrm{m}}(s|\omega) \stackrel{\text{def}}{=} \phi(s|\omega, \omega), \omega \in \mathcal{P}, \tag{1}$$

and the nonmated similarity score PDF of the same probe identity by

$$\phi_{\mathrm{nm}}(s|\omega) \stackrel{\text{def}}{=} \frac{1}{|\mathcal{P}| - 1} \sum_{\nu \in \mathcal{P}, \nu \neq \omega} \phi(s|\omega, \nu), \tag{2}$$

with $|\mathcal{P}|$ size of the population $\mathcal{P}$. This represents the PDF of the nonmated similarity score of a probe from ω compared with a reference from an unknown random identity. The global mated and nonmated similarity score PDFs over the population, representing similarity score PDFs from unknown random probe and reference identities, are then given by, respectively,

$$\phi_{\mathrm{m}}(s) = \frac{1}{|\mathcal{P}|} \sum_{\omega \in \mathcal{P}} \phi_{\mathrm{m}}(s|\omega), \tag{3}$$

$$\phi_{\mathrm{nm}}(s) = \frac{1}{|\mathcal{P}|} \sum_{\omega \in \mathcal{P}} \phi_{\mathrm{nm}}(s|\omega). \tag{4}$$

The biometric comparator compares $s = \mathrm{s}(\chi, y)$ to a threshold t to determine whether χ and y originate from the same identity or not. The *false-match probability* $p_{\mathrm{fm}}(t|\omega)$ and *true-match probability* $p_{\mathrm{tm}}(t|\omega)$ of identity ω at similarity score threshold t are defined by

$$p_{\mathrm{fm}}(t|\omega) \stackrel{\text{def}}{=} \int_{s>t} \phi_{\mathrm{nm}}(s|\omega)\mathrm{d}s, \tag{5}$$

$$p_{\mathrm{tm}}(t|\omega) \stackrel{\text{def}}{=} \int_{s>t} \phi_{\mathrm{m}}(s|\omega)\mathrm{d}s, \tag{6}$$

respectively. The global false-match probability $p_{\mathrm{fm}}(t)$ and the true-match probability $p_{\mathrm{tm}}(t)$ are then given by

$$p_{\mathrm{fm}}(t) = \frac{1}{|\mathcal{P}|} \sum_{\omega \in \mathcal{P}} p_{\mathrm{fm}}(t|\omega), \tag{7}$$

$$p_{\mathrm{tm}}(t) = \frac{1}{|\mathcal{P}|} \sum_{\omega \in \mathcal{P}} p_{\mathrm{tm}}(t|\omega), \tag{8}$$

respectively. Note that the false- and true-match probabilities are properties of the similarity score taken as a random variable, while the FMR and TMR are empirical entities measured from realisations of the random similarity scores and can be seen as estimates for the false- and true-match probabilities, respectively.

The probabilistic ROC of a biometric comparison function is defined as the true-match probability presented as a function of the false-match probability. For an identity ω we define the individual probabilistic ROC by

$$\rho(\alpha|\omega) \stackrel{\text{def}}{=} p_{\text{tm}}(t|\omega)\Big|_{p_{\text{fm}}(t|\omega)=\alpha}, \tag{9}$$

The symbol α will be used for the false-match probability as the dependent variable in a probabilistic ROC. The global probabilistic ROC is defined by

$$\rho(\alpha) \stackrel{\text{def}}{=} p_{\text{tm}}(t)\Big|_{p_{\text{fm}}(t)=\alpha}. \tag{10}$$

The empirical ROC that is obtained in an evaluation experiment can be seen as an estimate for the global probabilistic ROC.

The average probabilistic ROC, obtained by (vertically) averaging individual probabilistic ROCs over a constant false-match probability will also be needed in Section IV. It is defined by

$$\overline{\rho}(\alpha) \stackrel{\text{def}}{=} \frac{1}{|\mathcal{P}|} \sum_{\omega \in \mathcal{P}} \rho(\alpha|\omega). \tag{11}$$

Note that in general $\rho(\alpha) \neq \overline{\rho}(\alpha)$. However, the following property describes an important case for which $\rho(\alpha) = \overline{\rho}(\alpha)$:

$$p_{\text{fm}}(t|\omega) = p_{\text{fm}}(t) \Rightarrow \rho(\alpha) = \overline{\rho}(\alpha). \tag{12}$$

The proof is given in Appendix A. Vertical averaging of ROCs is discussed in [22].

In closed-set identification, a gallery $\mathcal{G}$ of size n is a set of references y_i, $i = 1, \ldots, n$, with corresponding identities ω_i, $i = 1, \ldots, n$, i.e.,

$$\mathcal{G} \stackrel{\text{def}}{=} \bigcup_{i=1}^{n} \{\omega_i, y_i\}, \tag{13}$$

where each reference originates from a different identity, randomly drawn without replacement from the population $\mathcal{P}$. The r-best list of a probe χ contains the identities of the r pairs $\{\omega_i, y_i\} \in \mathcal{G}$ with the largest similarity scores $s(\chi, y_i)$. In closed-set identification, the individual probabilistic CMC denoted by $\text{cmc}(r|\omega; n)$ quantifies for $r = 1, \ldots, n$ the probabilities that ω is in the r-best list of a gallery of size n, containing $\{\omega, y\}$ and $n - 1$ randomly drawn pairs $\{\omega_j, y_j\}$, with $\omega_j \neq \omega$. The global probabilistic CMC

$$\text{cmc}(r; n) = \frac{1}{|\mathcal{P}|} \sum_{\omega \in \mathcal{P}} \text{cmc}(r|\omega; n) \tag{14}$$

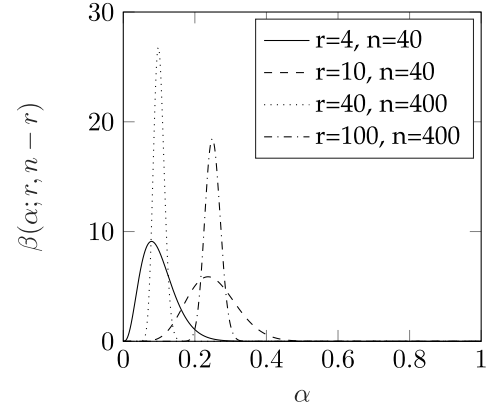then quantifies the probabilities that any probe represented in a randomly drawn gallery is in the r-best list.

Fig. 1.   Plots of $\beta(\alpha; r, n - r)$ for $(r, n) = (4, 40)$, $(10, 40)$ $(40, 400)$ $(100, 400)$.

IV. RELATING CMC AND ROC

As our main result, we present a compact relation between the probabilistic CMC and the probabilistic ROC, both for individual and global CMCs. For this, we need the β-PDF $\beta(x; a, b)$ [23] with parameters $a \in \mathbb{N}$ and $b \in \mathbb{N}$:

$$\beta(x; a, b) \stackrel{\text{def}}{=} \begin{cases} \frac{(a+b-1)!}{(a-1)!(b-1)!} x^{a-1}(1-x)^{b-1}, & 0 \leq x \leq 1, \\ 0, & \text{otherwise.} \end{cases} \tag{15}$$

In Bayesian statistics the β-PDF is used to model probability parameters such as that of the binomial distribution [23]. Here it appears naturally in the derivation of our main result. Its expectation and variance are given in Section V. Examples of β-PDFs are shown in Figure 1.

The following theorem expresses the probabilistic CMC as a functional on the probabilistic ROC with the β-PDF as a kernel. The proof is given in Appendix B.

Theorem 1: Given (a) a gallery $\mathcal{G}$ of size n, with one entry per identity, containing the entry $\{\omega, y\}$ for a probe identity ω and $n - 1$ other entries randomly drawn from the population of identities, and (b) a biometric comparison system for identity ω is characterised by a probabilistic ROC $\rho(\alpha|\omega)$. Then the individual probabilistic CMC $\text{cmc}(r|\omega; n)$ and the global probabilistic CMC $\text{cmc}(r; n)$ are given by, respectively,

$$\text{cmc}(r|\omega; n) = \begin{cases} \int_0^1 \rho(\alpha|\omega)\beta(\alpha; r, n - r)\mathrm{d}\alpha, & 1 \leq r < n, \\ 1, & r = n. \end{cases} \tag{16}$$

$$\text{cmc}(r; n) = \begin{cases} \int_0^1 \overline{\rho}(\alpha)\beta(\alpha; r, n - r)\mathrm{d}\alpha, & 1 \leq r < n, \\ 1, & r = n, \end{cases} \tag{17}$$

with $\overline{\rho}(\alpha)$ defined in Equation (11).

Figure 1 plots examples of the kernels $\beta(\alpha; r, n - r)$ in Equation (16) and Equation (17) as a function of α for $(r, n) = (4, 40)$, $(10, 40)$, $(40, 400)$, $(100, 400)$. These kernels act as local weighing functions on the probabilistic ROC, which provides more insight in the relation between the probabilistic CMC and ROC. We observe that the two graphs $(r, n) = (4, 40)$ and $(r, n) = (40, 400)$, with *fractional rank* $\frac{r}{n} = \frac{1}{10}$ as well as for the two graphs $(r, n) = (10, 40)$ and $(r, n) = (100, 400)$, with fractional rank $\frac{r}{n} = \frac{1}{4}$, the graphs remain more or less in the same position, but become narrower with increasing gallery size n. This convergence behaviour will be further discussed in Section V.

Summarising, we conclude that Equation (16) shows, in a compact form, that the individual probabilistic ROC contains all the information needed to compute an individual probabilistic CMC. Expression (17) gives a compact relation between the global probabilistic CMC that is often estimated as a performance indicator in experiments, and the average probabilistic ROC $\overline{\rho}(\alpha)$. The predictions of the CMCs in [8], [9], [10] are based on applying Equation (33) (in Appendix) to experimental FMRs and TMRs that are obtained by averaging over fixed thresholds, which is common in biometric evaluations. However, this would correspond to using the global ROC $\rho(\alpha)$ in Equation (17) for prediction of the CMC, instead of $\overline{\rho}(\alpha)$. The global ROC $\rho(\alpha)$, as we will also show in Section VI, may differ from $\overline{\rho}(\alpha)$ and this, in our view, explains the discrepancies between predicted and measured CMCs that have been observed in [8], [9], [10], [11], [12], [13], [14].

In [8], [20] it was shown that individual score normalisation improved the prediction of the CMC. This can be explained as follows. As a result of individual score normalisation, all identities will have similar FMRs. Then, according to Equation (12), the global ROC will become more similar to the average ROCs well and the prediction of the CMC will become better.

V. CONVERGENCE PROPERTIES

We observed in Figure 1 that for a constant fractional rank the kernels maintain their positions on the α-axis, but become narrower. This behaviour is easily explained by the expectation and variance of the β-PDF $\beta(x; r, n-r)$, which are given by, respectively,

$$\mathrm{E}\{x\} = \frac{r}{n}, \tag{18}$$

$$\mathrm{E}\left\{\left(x - \frac{r}{n}\right)^2\right\} = \frac{1}{n+1}\left(\frac{r}{n}\right)\left(1 - \frac{r}{n}\right). \tag{19}$$

Informally speaking, one can say that for increasing n and a fixed fractional rank $\frac{r}{n}$, $\beta(\alpha; r, n-r)$ will converge to a Dirac impulse function $\delta(\alpha - \frac{r}{n})$. Therefore, for large n and fixed $\frac{r}{n}$, the integral in Equation (16) effectively comes down to sampling the $\rho(\alpha|\omega)$ at $\alpha = \frac{r}{n}$, which implies that the shape of the individual CMC as a function of fractional rank converges to the individual ROC for large galleries. This is illustrated by Figure 2, which plots cmc$(r|\omega; n)$ for $n = 30, 60, 120$ as a function of fractional rank $\frac{r}{n}$ for $\rho(\alpha|\omega) = (1 - \exp(-50\alpha))/(1 - \exp(-50))$. Formally, we have the following theorem.

Theorem 2: Given (a) a gallery $\mathcal{G}$ of size n, with one entry per identity, containing the entry $\{\omega, y\}$ for a probe identity ω and $n-1$ other entries randomly drawn from the population of identities, and (b) a biometric comparison system that for identity ω is characterised by a probabilistic ROC $\rho(\alpha|\omega)$. Then the individual probabilistic CMC cmc$(r|\omega; n)$ and the global probabilistic CMC cmc$(r; n)$ are given by, respectively,

$$\mathrm{cmc}(r|\omega; n) = \begin{cases} \rho\left(\frac{r}{n}|\omega\right) + \mathrm{O}\left(\frac{1}{n}\right), & 1 \le r < n, \\ 1, & r = n, \end{cases} \tag{20}$$
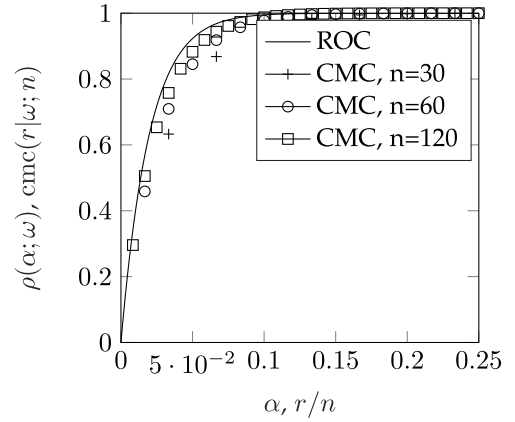

Fig. 2. Plots of $\rho(\alpha|\omega)$ as a function of α and cmc$(r|\omega; n)$ as a function of fractional rank $\frac{r}{n}$ for $n = 30, 60, 120$, illustrating how the individual CMC converges to the individual ROC.

$$\mathrm{cmc}(r; n) = \begin{cases} \overline{\rho}\left(\frac{r}{n}\right) + \mathrm{O}\left(\frac{1}{n}\right), & 1 \le r < n, \\ 1, & r = n. \end{cases} \tag{21}$$

In Equation (20) $\mathrm{O}(\frac{1}{n})$ is the Landau symbol that bounds the rate of convergence [24].

The proof is given in Appendix D.

From Theorem 2 it follows that for large galleries the probabilistic CMC indeed converges at a rate $1/n$ to the (average) probabilistic ROC. Note that the last but one line of Equation (43) in the proof implies that: (a) the rate of convergence is close to $1/n^2$ for ranks close to 1; (b) the rate of convergence decreases where the bend in the ROC is sharpest, because there the second derivative is largest; and (c) the approximation becomes perfect when the ROC flattens off, because there the second derivative vanishes. The convergence behaviour is summarised in the following corollary.

Corollary 1: Given (a) a gallery $\mathcal{G}$ of size n, with one entry per identity, containing the entry $\{\omega, y\}$ for a probe identity ω and $n-1$ other entries randomly drawn from the population of identities, and (b) a biometric comparison system that for identity ω is characterised by a probabilistic ROC $\rho(\alpha|\omega)$. Then the individual probabilistic CMC cmc$(r|\omega; n)$ and the global probabilistic CMC cmc$(r; n)$ satisfy, respectively,

$$\lim_{n \to \infty} \mathrm{cmc}(r|\omega; n) = \rho\left(\frac{r}{n}|\omega\right), \tag{22}$$

$$\lim_{n \to \infty} \mathrm{cmc}(r; n) = \overline{\rho}\left(\frac{r}{n}\right). \tag{23}$$

The proof follows on taking the limit $n \to \infty$ in Equation (22) and Equation (23).

In Figure 2, we observe that the probabilistic CMC approximates the probabilistic ROC from below. This is generally true for individual and average probabilistic ROCs that are concave, which is a desired property for an ROC.

The area under the ROC, i.e., $\int_0^1 \rho(\alpha|\omega)\mathrm{d}\alpha$ or $\int_0^1 \rho(\alpha)\mathrm{d}\alpha$, is often used to quantify the performance of a biometric comparison system [25], [26]. The closer it is to 1, the more discriminative the system is. For a CMC plotted as a function of fractional rank, a similar property is desirable. The curve should be close to the point $(0, 1)$ in the $(\frac{r}{n}, \mathrm{cmc})$-plane, which will be achieved if the area under the CMC, defined

as $\frac{1}{n}\sum_{r=1}^{n}\text{cmc}(r|\omega;n)$ is close to 1. The following corollary relates the area under the ROC with the that under the CMC, showing that for large galleries both requirements are equivalent. The proof is in Appendix E. In a somewhat different form this result is also presented in [9], Eq. 22].

Corollary 2: Given (a) a gallery $\mathcal{G}$ of size n, with one entry per identity, containing the entry $\{\omega, y\}$ for a probe identity ω and $n-1$ other entries randomly drawn from the population of identities, and (b) a biometric comparison system that for identity ω is characterised by a probabilistic ROC $\rho(\alpha|\omega)$. Then the average individual probabilistic CMC $\text{cmc}(r|\omega;n)$ and the average global probabilistic CMC $\text{cmc}(r;n)$ are given by, respectively,

$$\frac{1}{n}\sum_{r=1}^{n}\text{cmc}(r|\omega;n) = \left(1 - \frac{1}{n}\right)\int_{0}^{1}\rho(\alpha|\omega)\mathrm{d}\alpha + \frac{1}{n}, \quad (24)$$

$$\frac{1}{n}\sum_{r=1}^{n}\text{cmc}(r;n) = \left(1 - \frac{1}{n}\right)\int_{0}^{1}\overline{\rho}(\alpha)\mathrm{d}\alpha + \frac{1}{n}, \quad (25)$$

Hence,

$$\lim_{n\to\infty}\frac{1}{n}\sum_{r=1}^{n}\text{cmc}(r|\omega;n) = \int_{0}^{1}\rho(\alpha|\omega)\mathrm{d}\alpha, \quad (26)$$

$$\lim_{n\to\infty}\frac{1}{n}\sum_{r=1}^{n}\text{cmc}(r;n) = \int_{0}^{1}\overline{\rho}(\alpha)\mathrm{d}\alpha. \quad (27)$$

So far, theoretical relations between the probabilistic ROC and CMC have been derived. In Section VI these results will be illustrated by experiments that produce empirical ROCs and CMCs.

VI. ILLUSTRATIVE EXPERIMENTS

The goal of the experiments is to illustrate the validity of Theorems 1 and 2. In order to do that, we will estimate empirical ROCs and CMCs from data, use Equation (16) and Equation (17) to predict CMCs form them, and compare these with the empirical CMCs.

We will first present experiments based on synthetically generated random biometric samples. In this way we generate sufficient samples to produce accurate ROCs and CMCs. Second, we will present experiments on real data, namely the FRGC-V2 facial image dataset [17], using samples from identities that contributed a larger number of 20 samples, and the FVC2006 fingerprint dataset [18] and The Hong Kong Polytechnic University (HKPU) Cross-Spectral Iris Images Database [19], both using samples from identities that contributed 10 samples.

In the previous sections we worked with probabilistic ROCs and CMCs, which follow from the underlying probability density functions of similarity scores. In the current section, we will work with empirical ROCs and CMCs and, formally, we should introduce new notation for that. In order to avoid notational complexity, we will not do that, except for the CMCs that are predicted from the empirical ROCs, which we will denote as $\widehat{\text{cmc}}(r|\omega;n)$ and $\widehat{\text{cmc}}(r;n)$.

The synthetic and the real-data experiments follow the same approach for the computation of the ROCs and CMCs. Starting point is a dataset containing features of n identities $\omega = 1, \ldots, n$, with m features $\mathbf{x}_{\omega,j}$, $j = 1, \ldots, m$ per identity. For each identity ω we compute a set $\mathcal{S}_{m,\omega} = \{s(\mathbf{x}_{\omega,j}, \mathbf{x}_{\omega,l})|(j, l) \in \{1, \ldots, j\}^2, l < j\}$ with $\frac{1}{2}m(m-1)$ mated similarity scores, and set $\mathcal{S}_{nm,\omega} = \{s(\mathbf{x}_{\omega,j}, \mathbf{x}_{\nu,l})|\nu \neq \omega, (j, l) \in \{1, \ldots, j\}^2\}$ with $(n-1)m^2$ nonmated similarity scores.

The empirical ROC $\rho(\alpha|\omega)$ is computed as a piecewise linear function connecting points $(\alpha(t_i), \rho(\alpha(t_i)))$, with

$$\alpha(t_i) \overset{\text{def}}{=} \frac{|\{s|s \in \mathcal{S}_{nm,\omega}, s \geq t_i\}|}{(n-1)m^2}, \quad (28)$$

$$\rho(\alpha(t_i)) \overset{\text{def}}{=} \frac{|\{s|s \in \mathcal{S}_{m,\omega}, s \geq t_i\}|}{\frac{1}{2}m(m-1)}, \quad (29)$$

and $t_i \in \mathcal{S}_{m,\omega}$, $t_i > t_{i-1}$. If for some t_i and t_j we have that $\alpha(t_i) = \alpha(t_j)$, then only the pair $(\alpha(t_i), \rho(\alpha(t_i)))$ with maximum $\rho(\alpha(t_i))$ is retained. The global empirical ROC $\rho(\alpha)$ is computed in a similar (standard) way as the individual empirical ROCs, but based on aggregated sets of mated and nonmated similarity scores.

From the empirical ROCs $\rho(\alpha|\omega)$, $\omega = 1, \ldots, n$, we predict the individual CMCs $\widehat{\text{cmc}}(r|\omega;n)$ by numerically evaluating Equation (16). We compute the average individual empirical ROC $\overline{\rho}(\alpha)$ by averaging the individual empirical ROCs $\rho(\alpha|\omega)$, $\omega = 1, \ldots, n$, and the predicted CMC $\widehat{\text{cmc}}(r;n)$ by averaging the individual predicted CMCs $\widehat{\text{cmc}}(r|\omega;n)$, $\omega = 1, \ldots, n$.

We also use the similarity scores to compute individual empirical CMCs $\text{cmc}(r|\omega;n)$ for all identities ω. We do this by mimicking a large number of identifications. For identity ω and every sample index i, $n-1$ nonmated similarity scores $s(\mathbf{x}_{\omega,i}, \mathbf{x}_{\nu,j_\nu})$, $\nu = 1, \ldots, m$, $\nu \neq \omega$, with each j_ν randomly drawn from $\{1, \ldots, m\}$ are selected. Then, for $m-1$ mated similarity scores $s(\mathbf{x}_{\omega,i}, \mathbf{x}_{\omega,j})$, $j = 1, \ldots, m$, $j \neq i$, the set $\{s(\mathbf{x}_{\omega,i}, \mathbf{x}_{\omega,j}), \{s(\mathbf{x}_{\omega,i}, \mathbf{x}_{\nu,j_\nu})\}_{\nu \neq \omega}\}$ is sorted in descending order and the ranks of the mated similarity score $s(\mathbf{x}_{\omega,i}, \mathbf{x}_{\omega,j})$ are collected in a histogram with bins $1, \ldots, n$. This mimics identification in a gallery of size n with a mated enrolled feature vector $\mathbf{x}_{\omega,i}$ and $n-1$ nonmated enrolled feature vectors $\mathbf{x}_{\nu,j_\nu}$, $\nu = 1, \ldots, m$, $\nu \neq \omega$ with probes $\mathbf{x}_{\omega,j}$, $j =, \ldots, m$, $j \neq i$. In order to increase the accuracy of the individual empirical CMC this is done m_g times for every sample index i of identity ω by randomly drawing m_g sets $\{s(\mathbf{x}_{\omega,i}, \mathbf{x}_{\nu,j_\nu})\}_{\nu \neq \omega}$ of nonmated similarity scores. Each time the rank histogram is updated. Per identity ω a CMC is computed from the histogram, based on $m_g m(m-1)$ rankings of similarity scores. The global empirical CMC $\text{cmc}(r;n)$ is computed by averaging the individual CMCs $\text{cmc}(r|\omega;n)$. The experimental parameters n (gallery size), m (the number of features per identity), and m_g (the number of randomly drawn galleries per mated gallery entry) are specified in Table I.

We will present the results in three types of graphs: 1) Figures with individual empirical performance characteristics, in particular individual empirical ROCs $\rho(\alpha|\omega)$, the corresponding individual predicted CMCs $\widehat{\text{cmc}}(r|\omega;n)$, and the individual empirical CMCs $\text{cmc}(r|\omega;n)$; 2) Figures with global empirical performance characteristics, i.e., the empirical ROC $\rho(\alpha)$, the average individual empirical ROC $\overline{\rho}(\alpha|\omega)$,

TABLE I
PARAMETER VALUES FOR THE EXPERIMENTS: GALLERY SIZE n, #FEATURES/IDENTITY m, #GALLERIES/MATED ENTRY m_g

data		n	m	m_g
synthetic data		10	30	30
		100	20	5
FRGC-V2 data		10	20	30
		100	20	5
FVC2006 data		100	10	30
HKPU Cross-Spectral Iris data		100	10	30

the global predicted CMC $\widehat{\text{cmc}}(r; n)$, and the global empirical CMC $\text{cmc}(r; n)$; 3) Figures that provide a direct comparison between $\text{cmc}(r; n)$ and $\widehat{\text{cmc}}(r; n)$. CMCs and ROCs are plotted in one graph in order to illustrate their relation. For that purpose the CMC is plotted as a function of fractional rank $\frac{r}{n}$.

A. Synthetic Data

We simulate a simplified biometric feature comparison, based on Gaussian between- and within-identity variations. Let $\mathbf{x} = \mathbf{b} + \mathbf{w}$ be a feature vector of an identity, with $\mathbf{b} \sim N(\mathbf{0}, \Sigma_B)$ the individual feature mean and $\mathbf{w} \sim N(\mathbf{0}, \Sigma_W)$ modelling the within-identity variations. In our synthetic-data experiments $\mathbf{x} \in \mathbb{R}^4$ and Σ_B is a diagonal covariance matrix with diagonal elements

$$\left(\sigma_1^2, \ldots, \sigma_4^2\right) = (0.5, 0.8, 0.85, 0.9). \tag{30}$$

Furthermore, $\Sigma_W = \mathbf{I} - \Sigma_B$, such that $\mathbf{x} \sim N(\mathbf{0}, \mathbf{I})$.

For each of the n identities in the gallery, we randomly draw one mean vector $\mathbf{b}_\omega$, $\omega = 1, \ldots, n$ and m vectors $\mathbf{w}_{\omega,j}$, $\omega = 1, \ldots, n$, $j = 1, \ldots, m$ resulting in m vectors $\mathbf{x}_{\omega,j}$ per identity. From this synthetic dataset we compute all relevant similarity scores $s(\mathbf{x}_{\omega,j}, \mathbf{x}_{v,l})$, $(\omega, j) \neq (v, l)$.

Individual empirical ROCs, individual predicted CMCs, individual empirical CMCs, the average individual empirical ROC, the empirical ROC, and the empirical CMC are computed for gallery sizes $n = 10$ and $n = 100$ and for 2 classifiers: the log-likelihood-ratio classifier optimised for the data and the cosine-similarity classifier. For each combination of gallery size and classifier a new data set is randomly generated. The experimental parameters are given in Table I.

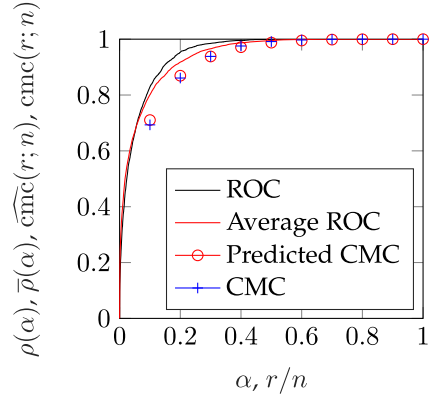The log-likelihood-ratio classifier computes a similarity score

$$s(\mathbf{x}_{\omega,j}, \mathbf{x}_{v,l}) = -\frac{1}{2} \sum_{d=1}^{D} \log\left(1 - \sigma_d^4\right)$$
$$- \frac{1}{4} \sum_{d=1}^{D} \frac{\sigma_d^2}{1 - \sigma_d^2}\left((\mathbf{x}_{\omega,j})_d - (\mathbf{x}_{v,l})_d\right)^2$$
$$+ \frac{1}{4} \sum_{d=1}^{D} \frac{\sigma_d^2}{1 + \sigma_d^2}\left((\mathbf{x}_{\omega,j})_d + (\mathbf{x}_{v,l})_d\right)^2, \tag{31}$$

with $D = 4$ and σ_d^2 specified in Equation (30). The cosine-similarity classifier computes a similarity score
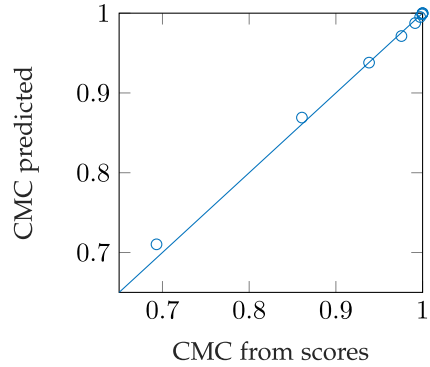
$$s(\mathbf{x}_{\omega,j}, \mathbf{x}_{v,l}) = \frac{\mathbf{x}_{\omega,j}^{\mathrm{T}} \mathbf{x}_{v,l}}{\|\mathbf{x}_{\omega,j}\| \|\mathbf{x}_{v,l}\|}. \tag{32}$$
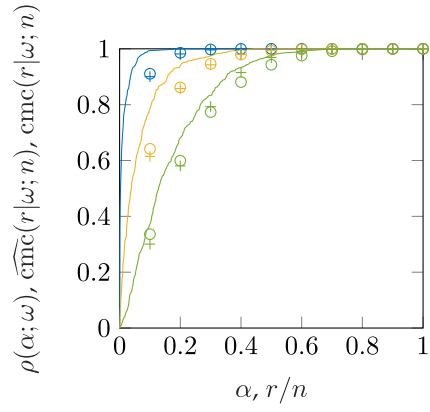
(a) Selection of 3 individual empirical ROCs (solid lines) and corresponding individual predicted CMCs ('o') and individual empirical CMCs ('+').

(b) Empirical ROC (black solid line), average individual empirical ROC (red solid line), predicted CMC ('o'), and empirical CMC('+').

(c) Empirical vs. predicted CMC.

Fig. 3. Synthetic-data experiments. Gallery size $n = 10$, log-likelihood-ratio classifier.

Figures 3(a), 3(b), and 3(c) show the results for gallery size $n = 10$ with the log-likelihood-ratio classifier. Figure 3(a) shows 3 of the 10 individual empirical ROCs $\rho(\alpha|\omega)$ and the corresponding identity predicted CMCs $\widehat{\text{cmc}}(r|\omega; n)$ and the individual empirical CMCs $\text{cmc}(r|\omega; n)$. We see that there can be quite a spread between the individual empirical ROCs and that the individual predicted CMCs deviate slightly from the individual empirical CMCs, but this deviation is reduced if we consider the global predicted CMC $\widehat{\text{cmc}}(r; n)$ and the global empirical CMC $\text{cmc}(r; n)$ in Figure 3(b). This figure

also shows that the empirical ROC $\rho(\alpha)$ and the average individual empirical ROC $\overline{\rho}(\alpha|\omega)$ are different. Figure 3(c) directly compares the empirical CMC with the predicted CMC, showing that the deviation is largest at lower rank values.

Figures 4(a), 4(b), and 4(c), show the results for gallery size $n = 10$ with the cosine-similarity classifier. The observations are mainly similar to those made for gallery size $n = 10$ with the log-likelihood-ratio classifier. The main difference is that here the empirical ROC $\rho(\alpha)$ and the average individual empirical ROC $\overline{\rho}(\alpha|\omega)$ in Figure 4(b) are more similar for the cosine-similarity classifier.

Figures 5(a), 5(b), and 5(c), show the results for gallery size $n = 100$ with the log-likelihood-ratio classifier. Here we can see that both the individual as well as the global empirical and predicted CMCs are closer together than in the $n = 10$ experiments. In fact, from Figure 5(c) we see that the predicted CMC approximates the empirical quite well. We can also observe that the empirical and predicted CMCs, plotted as functions of r/n more closely approximate the average ROCs as in the $n = 10$ experiments as was proved in Theorem 2. The empirical ROC $\rho(\alpha)$ is above the average individual empirical ROC $\overline{\rho}(\alpha)$, which is to be expected, because the log-likelihood-ratio classifier is the optimal classifier and the best recognition performance is obtained when the same log-likelihood-ratio threshold is used for all identities as was shown in [27]. The average ROC is obtained by setting the threshold such that all identities have the same false-match rate, which leads to a different log-likelihood-ratio threshold for each identity. This effect was also visible for the $n = 10$ case, but not for the entire ROC. We expect this observation because ROCs obtained with only 10 identities are less accurate than ROCs obtained with 100 identities. Figures 6(a), 6(b), and 6(c), show the results for gallery size $n = 100$ with the cosine-similarity classifier. Again, the observations are mainly similar to those made for gallery size $n = 100$ with the log-likelihood-ratio classifier. The main difference is again that here the empirical ROC $\rho(\alpha)$ and the average individual empirical ROC $\overline{\rho}(\alpha|\omega)$ in Figure 6(b) are more similar for the cosine-similarity classifier. In fact, they seem to overlap completely. We assume that this is because in the given constellation of feature vectors $\mathbf{x} \sim N(\mathbf{0}, \mathbf{I})$ and the cosine-similarity classifier, we have the nonmated similarity scores that are equally distributed, i.e., $\phi_{\mathrm{nm}}(s|\omega) = \phi_{\mathrm{nm}}(s)$, then according to Equation (12) the average ROC coincides with the global ROC.

The above experiments confirm our main result, laid down in Theorem 1, that the CMC can be predicted from the average ROC. For the smaller gallery size there are minor deviations at the lower rank values, that can be ascribed to inaccuracies of individual ROCs obtained with few samples.

B. Face Recognition Data

As our primary goal is illustrating the relation between the ROC and the CMC, we choose the FRGC-V2 face dataset [17], where the performance is not near-ideal. Though one can use LFW and alike datasets, we note that most of the newer face recognition systems provide near-ideal performance [28] on those, deeming them less useful for our purposes. The
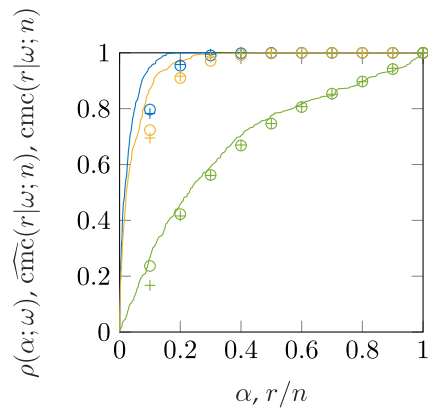
(a) Selection of 3 individual empirical ROCs (solid lines) and corresponding individual predicted CMCs ('o') and individual empirical CMCs ('+').
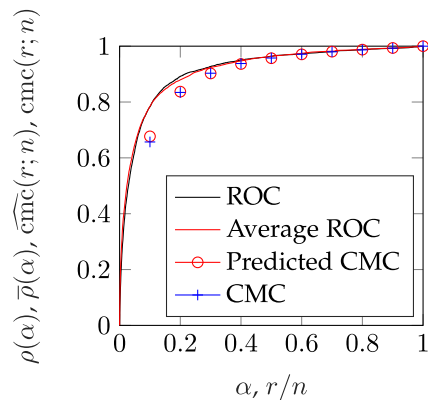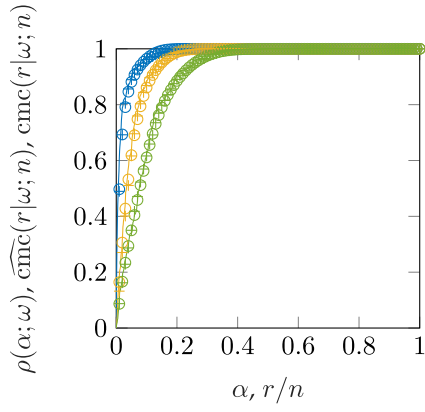

(b) Empirical ROC (black solid line), average individual empirical ROC (red solid line), predicted CMC ('o'), and empirical CMC('+').
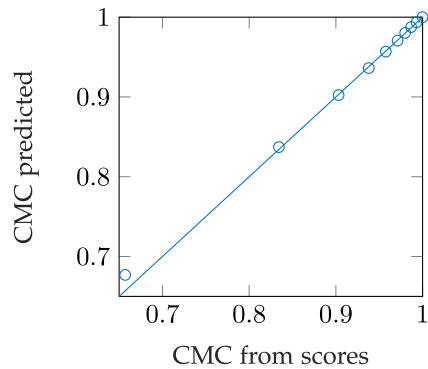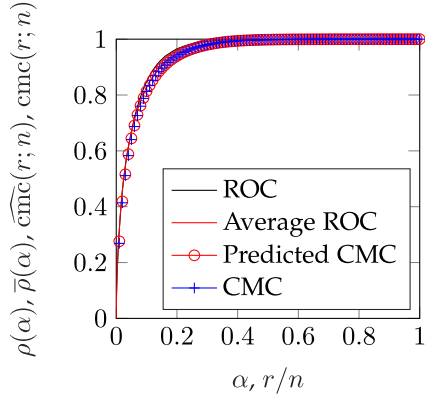

(c) Empirical vs. predicted CMC.

Fig. 4. Synthetic-data experiments. Gallery size $n = 10$, cosine-similarity classifier.
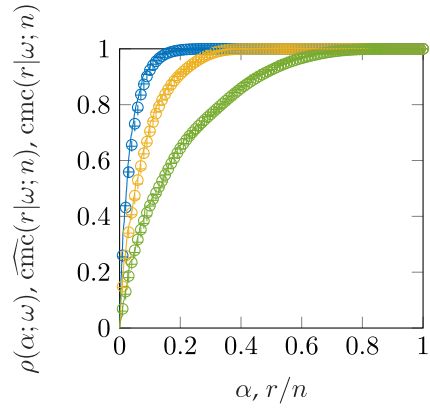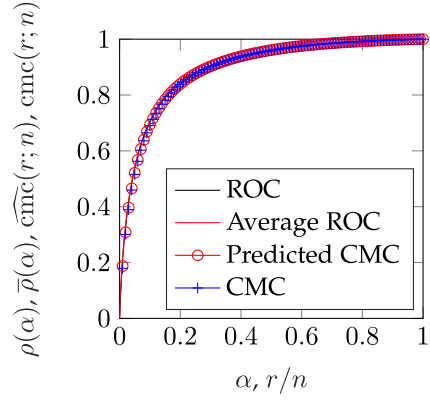
FRGC-V2 dataset consists of a training split of 222 unique identities and a testing split of 466 unique identities. We employ the testing split from which we preselect the 285 identities with at least 20 images. From these identities we randomly retain 20 images per identity. We further preprocess the images by detecting the face region with a tight cropping [29]. We extract features $\mathbf{x}_{\omega,j} \in \mathbb{R}^{512}$ and compute all the relevant similarity scores $\mathrm{s}(\mathbf{x}_{\omega,j}, \mathbf{x}_{v,l})$, $(\omega, j) \neq (v, l)$, using the pre-trained ElasticFace [30] face recognition system based on deep learning to extract the feature vectors.

(a) Selection of 3 individual empirical ROCs (solid lines) and corresponding individual predicted CMCs ('o') and individual empirical CMCs ('+').

(b) Empirical ROC (black solid line), average individual empirical ROC (red solid line), predicted CMC ('o'), and empirical CMC('+').
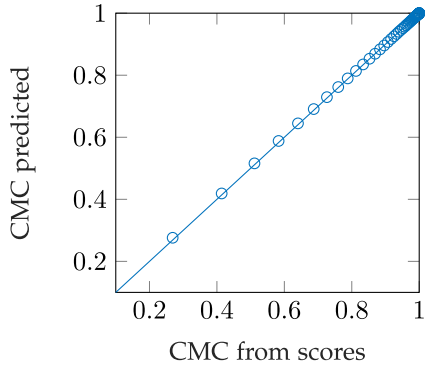
(c) Empirical vs. predicted CMC.

Fig. 5. Synthetic-data experiments. Gallery size $n = 100$, log-likelihood-ratio classifier.

(a) Selection of 3 individual empirical ROCs (solid lines) and corresponding individual predicted CMCs ('o') and individual empirical CMCs ('+').

(b) Empirical ROC (black solid line), average individual empirical ROC (red solid line), predicted CMC ('o'), and empirical CMC('+').

(c) Empirical vs. predicted CMC.

Fig. 6. Synthetic-data experiments. Gallery size $n = 100$, cosine-similarity classifier.

These are compared using the cosine-similarity classifier in Equation (32). The employed pre-trained models are trained on the MS1MV2 dataset [28] and validated on various datasets such as LFW, AgeDb-30, CPLFW, CALFW and CFP-FP for state-of-the-art performance.
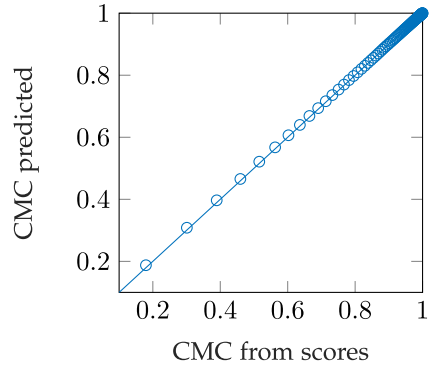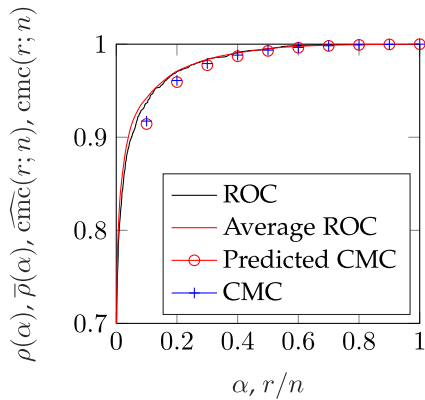
For gallery sizes $n = 10$ and $n = 100$, we randomly selected, respectively, 10 and 100 identities out of the pre-selected 285. In this way we have the same maximum numbers of identities and gallery sizes as in the synthetic-data

experiments described in Subsection VI-A. The experimental parameters are specified in Table I.

Figures 7(a), 7(b), and 7(c), show the results for gallery size $n = 10$. The results are similar to those obtained with synthetic data and gallery size $n = 10$. Figure 7(a) shows 3 from the 10 individual empirical ROCs $\rho(\alpha|\omega)$ and the corresponding individual predicted CMCs $\widehat{cmc}(r|\omega; n)$ and the individual empirical CMCs $cmc(r|\omega; n)$. As was the case with the synthetic data, there is spread between the individual empirical ROCs. The individual predicted CMCs deviate slightly from
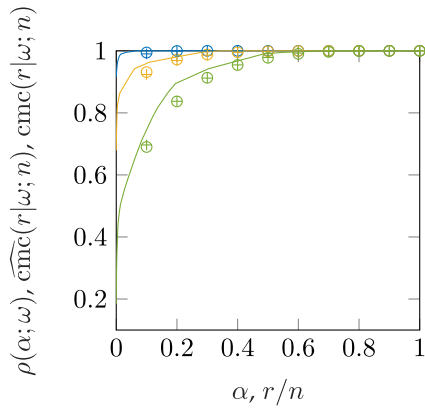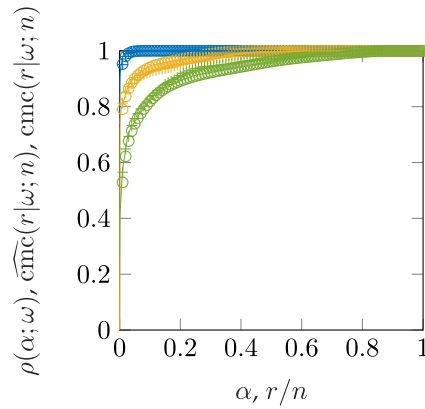
(a) Selection of 3 individual empirical ROCs (solid lines) and corresponding individual predicted CMCs ('o') and individual empirical CMCs ('+').
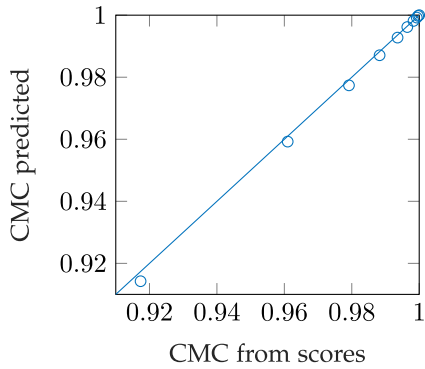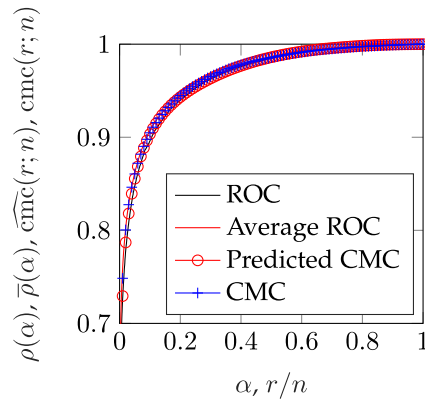

(b) Empirical ROC (black solid line), average individual empirical ROC (red solid line), predicted CMC ('o'), and empirical CMC('+').

(c) Empirical vs. predicted CMC.

Fig. 7. Face recognition data experiments. Gallery size $n = 10$, FRCG-V2 data [17], face recognition system: ElasticFace [30] with a cosine-similarity classifier.

(a) Selection of 3 individual empirical ROCs (solid lines) and corresponding individual predicted CMCs ('o') and individual empirical CMCs ('+').

(b) Empirical ROC (black solid line), average individual empirical ROC (red solid line), predicted CMC ('o'), and empirical CMC('+').
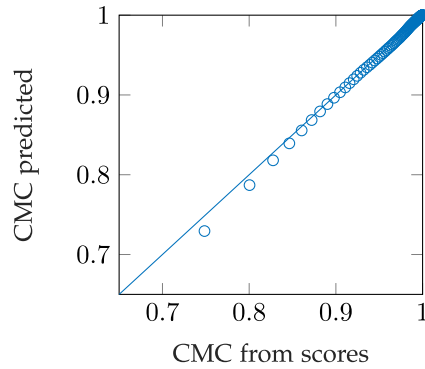

(c) Empirical vs. predicted CMC.

Fig. 8. Face recognition data experiments. Gallery size $n = 100$, FRCG-V2 data [17], face recognition system: ElasticFace [30] with a cosine-similarity classifier.

the individual empirical CMCs, but this deviation is reduced if we consider the global predicted CMC $\widehat{\text{cmc}}(r; n)$ and the global empirical CMC $\text{cmc}(r; n)$ in Figure 7(b). This figure also shows that the empirical ROC $\rho(\alpha)$ and the average individual empirical ROC $\overline{\rho}(\alpha|\omega)$ are different. Figure 7(c) directly compares the empirical CMC with the predicted CMC, showing that the deviation is largest at lower rank values.

Figures 8(a), 8(b), and 8(c), show the results for gallery size $n = 100$. Figure 8(a) shows 3 from the 100 individual

empirical ROCs $\rho(\alpha|\omega)$ and the corresponding individual predicted CMCs $\widehat{\text{cmc}}(r|\omega; n)$ and the individual empirical CMCs $\text{cmc}(r|\omega; n)$. There is spread between the individual empirical ROCs and the individual predicted CMCs deviate slightly from the individual empirical CMCs, but this deviation is reduced if we consider the global predicted CMC $\widehat{\text{cmc}}(r; n)$ and the global empirical CMC $\text{cmc}(r; n)$ in Figure 8(b). This figure also shows that the empirical ROC $\rho(\alpha)$ and the average individual empirical ROC $\overline{\rho}(\alpha|\omega)$ are different. Figure 8(c) directly compares the empirical CMC with the predicted CMC,

showing that the deviation is largest at lower rank values where the predicted CMC underestimates the empirical one. This was not the case for the synthetic data and also not for the face recognition data experiments with gallery size $n = 10$. We expect this for lower values of α as the individual and average ROCs are much steeper for the face recognition data experiments than for those on synthetic data. Since only few data points are available for lower values of α, the concave ROCs are systematically underestimated when Equation (16) is applied to the piecewise linear approximation of the ROCs, leading to underestimation of the predicted CMCs. For gallery size $n = 10$, the ROC is less steep, and more data points are available, therefore the piecewise linear approximation of the ROC is more accurate.

As was the case with the synthetic-data experiments, the experiments in this subsection confirm our main result, laid down in Theorem 1, that the CMC can be predicted from the average ROC. In steeper parts of the ROC there are deviations in the prediction that can be ascribed to the combination of the availability of fewer datapoints and the piecewise linear approximation of the individual and average ROCs.
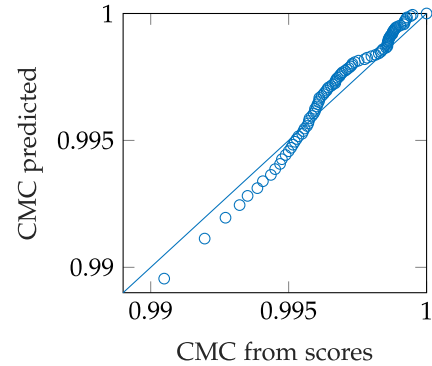
C. Fingerprint Recognition Data

We employ set A of the DB2 subset of the Fingerprint Verification Competition 2006 [18]. This dataset was captured using an optical sensor and consists of 150 unique fingerprints with 12 samples per finger. The fingerprints correspond to images of size 400x560 represented in 256 gray levels in uncompressed format with a 569 dpi resolution. We choose a subset of 100 randomly selected fingerprints with 10 samples for each fingerprint. For each of the fingerprints, we extract minutiae using MINDTCT and compare the minutiae using Bozorth3 [31].

Because only 10 fingerprints per individual are available, there are only 45 mated comparisons to compute the individual empirical ROCs, which will result in empirical ROCs with a high granularity in the vertical coordinates. This will make the computation of individual predicted CMCs inaccurate. Therefore, we will only present the global empirical ROC, the average individual empirical ROC, the predicted global CMC, and the empirical CMC, for gallery size $n = 100$. For this larger gallery size, the inaccuracies in the individual empirical ROCs and CMCs average out in the global empirical ROCs and CMCs respectively.

Figure 9(a) shows the empirical ROC, the average individual ROC, the global predicted CMC $\widehat{\text{cmc}}(r; n)$ and the global empirical CMC $\text{cmc}(r; n)$, which are all close. This is to be expected because of the higher recognition performance. Figure 9(a) directly compares the empirical CMC with the predicted CMC, showing that at lower rank values the predicted CMC underestimates the empirical one somewhat, whereas at higher ranks it overestimates. We expect that, as was also mentioned in Section VI-B, that the underestimation at lower rank values is due to the steepness of this ROC. Note the scale of the axis, from which we can see that the prediction is close. Here, there is no underestimation of the CMC at lower rank
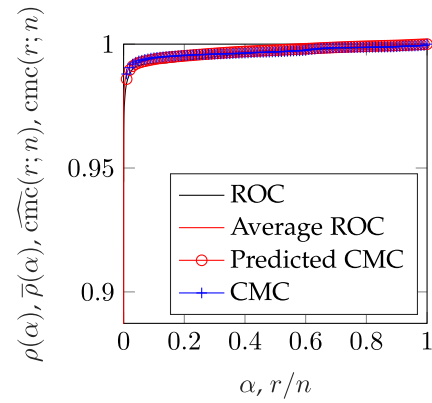
(a) Empirical ROC (black solid line), average individual empirical ROC (red solid line), predicted CMC ('o'), and empirical CMC('+').
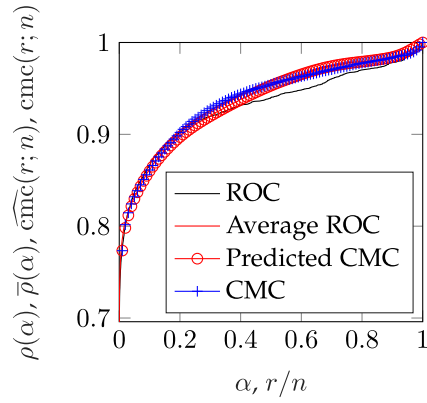

(b) Empirical vs. predicted CMC.

Fig. 9. Fingerprint recognition data experiments. Gallery size $n = 100$, FVC2006 data [18], fingerprint recognition system: MINDTCT with Bozorth3 [31].

values, which we ascribe to that this ROC is less steep than those for face and fingerprint recognition.
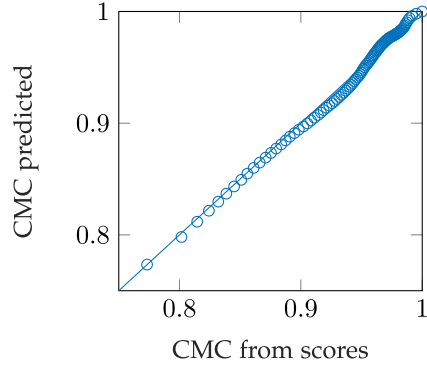
D. Iris Recognition Data

We use Near-Infra Red (NIR) iris image subset from The Hong Kong Polytechnic University Cross-Spectral Iris Images Database [19]. This database consists of total 12,540 iris images collected from left and right eyes of 209 subjects in two different spectrums (Visible and NIR) with 15 different instances. For the sake of our experiments, we consider a subset of images from 100 randomly selected subjects with 10 images from left eye each captured in NIR spectrum. For all the iris images, we segment and localize iris region following which we use Daugman's rubber sheet model [32], [33]. Further, we extract binarised 1D Log-Gabor codes from iris images as features and employ the fractional Hamming distance to compare two iris codes [32]. Formally, the fractional Hamming distance is a rational number and not a real number. However, the mated and nonmated probabilities can be approximated by continuous PDFs, which allows us to apply our results.

For the same reason as given for the fingerprint data in Section VI-C we only present the global empirical ROC, the average individual empirical ROC, the predicted global CMC, and the empirical CMC, for gallery size $n = 100$.

(a) Empirical ROC (black solid line), average individual empirical ROC (red solid line), predicted CMC ('o'), and empirical CMC('+').

(b) Empirical vs. predicted CMC.

Fig. 10. Iris recognition data experiments. Gallery size $n = 100$, HKPU Cross-Spectral Iris data [19]. Iris recognition system: binarised 1D Log-Gabor codes with fractional Hamming distance [32].

Figure 10(a) shows the empirical ROC, the average individual ROC, the global predicted CMC $\widehat{\text{cmc}}(r; n)$ and the global empirical CMC cmc$(r; n)$. We observe that the empirical ROC deviates somewhat from the other graphs, which are closer to each other. We can also see that the recognition performance is poor, with an equal error rate of about 15%. Figure 10(b) directly compares the empirical CMC with the predicted CMC, showing that the prediction is close.

VII. CONCLUSION

We extended earlier experimental and theoretical work [8], [9], [10], [11], [12], [13], [14] on the relation between the ROC and the CMC. Our main result is that, in a probabilistic framework, an individual's CMC can be predicted from the individual's ROC as a functional with a kernel based on the β-PDF. This result cannot be applied directly to verification and closed-set identification experiments to provide a relation between a global CMC and a global ROC for two reasons. The first is that the experimental ROC is based on counting true and false matches with similarity scores above fixed thresholds, while the established relation holds for ROCs obtained by averaging individual ROCs at fixed false-match rates. The second reason is that, if one should decide to compute individual ROCs to predict a CMC from, this would require a large number of mated similarity scores for each identity in the

gallery, to have the empirical ROC approximate the probabilistic one well enough. This is particularly true for the steeper parts of the ROC, determined by the tails of the similarity score distributions. The main result is complemented with convergence properties for increasing gallery size. In particular, we show that for increasing gallery size, the individual CMCs as a function of fractional rank, converge to the individual ROCs. Our results provide explanations for discrepancies related to the ROC and CMC observed in the literature.

The theory is illustrated by experiments on synthetic data with Gaussian within- and between-class variations, and on real data, namely the FRGC-V2 facial image dataset [17], the FVC2006 fingerprint dataset [18], and The Hong Kong Polytechnic University Cross-Spectral Iris Images Database [19]. The experiments confirm the theoretical results. It must be noted that the real-data experiments show that the prediction of the CMC from individual ROCs is less accurate where the ROC is steeper, due to less accurate estimation of the ROCs in the tails of the similarity score distributions.

Finally, because we found that there is a probability-theoretical relation between the individual ROCs averaged over fixed false-match rates and the global CMC, but generally not between the global ROC and CMC, we cannot conclude that experimental biometric results only need to be presented as ROCs and that CMCs would not have added value. However, we think that presenting ROCs has the advantage over presenting CMCs that an ROC is independent of the gallery size, and therefore lends itself better for a general comparison of biometric recognition performance.

APPENDIX A
PROOF OF EQUATION (12)

Lemma 1: Given a biometric comparison system that is characterized by $p_{\text{fm}}(t|\omega) = p_{\text{fm}}(t)$ then $\rho(\alpha) = \overline{\rho}(\alpha)$.
Proof:

$$
\begin{aligned}
\rho(\alpha) &= p_{\text{tm}}(t)|_{p_{\text{fm}}(t)=\alpha} \\
&= \frac{1}{|\mathcal{P}|} \sum_{\omega \in \mathcal{P}} p_{\text{tm}}(t)|_{p_{\text{fm}}(t)=\alpha} \\
&= \frac{1}{|\mathcal{P}|} \sum_{\omega \in \mathcal{P}} p_{\text{tm}}(t|\omega)|_{p_{\text{fm}}(t|\omega)=\alpha} \\
&= \frac{1}{|\mathcal{P}|} \sum_{\omega \in \mathcal{P}} \rho(\alpha|\omega) = \overline{\rho}(\alpha).
\end{aligned}
$$

∎

APPENDIX B
PROOF OF THEOREM 1

Proof: We start with the expression for the CMC

$$
\begin{aligned}
\text{cmc}(r|\omega; n) = \int_{\mathcal{S}} \sum_{l=1}^{r} \binom{n-1}{l-1} p_{\text{fm}}^{l-1}(s|\omega) \\
(1 - p_{\text{fm}}(s|\omega))^{n-l} \phi_{\text{m}}(s|\omega)\text{d}s, \quad (33)
\end{aligned}
$$

as derived in [8, p. 51], [10, eq. (16)], and [9, eq. (9)], under the implicit assumption that all identities in the gallery gave the

same ROC. To simplify the expression we rewrite the integrand using the β-PDF in Equation (15) and to include the case that $p_{\text{fm}}(s|\omega) \equiv 0$ and $p_{\text{tm}}(s|\omega) > 0$ for $s > s_0$, which will result is a jump in the ROC at $\alpha = 0$, we split Equation (33) into two parts:

$$\text{cmc}(r|\omega; n) = \int_{s > s_0} \frac{1}{n} \sum_{l=1}^{r} \beta(p_{\text{fm}}(s|\omega); l, n-l+1)\phi_{\text{m}}(s|\omega)ds$$
$$+ \int_{s \leq s_0} \frac{1}{n} \sum_{l=1}^{r} \beta(p_{\text{fm}}(s|\omega); l, n-l+1)\phi_{\text{m}}(s|\omega)ds. \tag{34}$$

Because $p_{\text{fm}}(s|\omega) \equiv 0$ for $s > s_0$, and $\beta(0; 1, n) = n$, and $\beta(0; l, n-l+1) = 0$ for $2 \leq l \leq n$, the first integral evaluates to $p_{\text{tm}}(s_0|\omega) = \rho(0|\omega)$, and

$$\text{cmc}(r|\omega; n) = \rho(0|\omega) + \int_{s \leq s_0} \frac{1}{n} \sum_{l=1}^{r} \beta(p_{\text{fm}}(s|\omega); l, n-l+1)$$
$$\phi_{\text{m}}(s|\omega)ds. \tag{35}$$

We change the integration variable s in Equation (35) into $\alpha = p_{\text{fm}}(s|\omega)$, with $\frac{d\alpha}{ds} = -\phi_{\text{nm}}(s|\omega)$, see Equation (5) and rewrite Equation (35) as

$$\text{cmc}(r|\omega; n) = \rho(0|\omega) + \int_{0}^{1} \rho'(\alpha|\omega)$$
$$\frac{1}{n} \sum_{l=1}^{r} \beta(\alpha; l, n-l+1)d\alpha. \tag{36}$$

Partial integration of the last term of Equation (36) yields

$$\text{cmc}(r|\omega; n) = \rho(0|\omega)$$
$$+ \left[\rho(\alpha|\omega)\frac{1}{n} \sum_{l=1}^{r} \beta(\alpha; l, n-l+1)\right]_{0}^{1}$$
$$- \int_{0}^{1} \rho(\alpha|\omega)\frac{1}{n} \sum_{l=1}^{r} \beta'(\alpha; l, n-l+1)d\alpha. \tag{37}$$

We have that $\beta(0; 1, n) = n$ and $\beta(0; l, n-l+1) = 0$ for $2 \leq l \leq n$. Also, $\beta(1; n, 1) = n$ and $\beta(1; l, n-l+1) = 0$ for $1 \leq l < n$. Therefore,

$$\left[\rho(\alpha|\omega)\frac{1}{n} \sum_{l=1}^{r} \beta(\alpha; l, n-l+1)\right]_{0}^{1}$$
$$= \begin{cases} \rho(1|\omega) - \rho(0|\omega), & r = n, \\ -\rho(0|\omega), & 1 \leq r < n. \end{cases} \tag{38}$$

The last line of Equation (37) can be simplified by using

$$\frac{1}{n} \sum_{l=1}^{r} \beta'(\alpha; l, n-l+1)$$
$$= \begin{cases} -\beta(\alpha; r, n-r), & 1 \leq r < n, \\ 0, & r = n, \end{cases} \tag{39}$$

which is proved in Appendix C. Substitution of Equation (38) and Equation (39) into Equation (37) and using $\rho(1|\omega) = 1$ yields Equation (16). The result for a global probabilistic CMC in Equation (17) follows by averaging both sides of Equation (16) over the probe identity population by using Equation (11) and Equation (14). ∎

APPENDIX C
PROOF OF EQUATION (39)

Lemma 2: Let $n \in \mathbb{N}$ and $l \in \mathbb{N}$, with $1 \leq l \leq n$, and let $\beta(\alpha; l, n-l+1)$ denote a β-PDF defined in Equation (15). Then

$$\frac{1}{n} \sum_{l=1}^{r} \beta'(\alpha; l, n-l+1)$$
$$= \begin{cases} -\beta(\alpha; r, n-r), & 1 \leq r < n, \\ 0, & r = n. \end{cases} \tag{40}$$

Proof: By using Equation (15) we have

$$\beta'(\alpha; l, n-l+1) = \begin{cases} -n\beta(\alpha; 1, n-1), & l = 1, \\ n\beta(\alpha; l-1, n-(l-1))- & \\ \qquad n\beta(\alpha; l, n-l), & 2 \leq l < n, \\ n\beta(\alpha; n-1, 1), & l = n. \end{cases} \tag{41}$$

Using Equation (41), we can rewrite the left-hand side of Equation (40) for $1 \leq r < n$ into

$$\frac{1}{n} \sum_{l=1}^{r} \beta'(\alpha; l, n-l+1)$$
$$= -\beta(\alpha; 1, n-1) +$$
$$\sum_{l=2}^{r}(\beta(\alpha; l-1, n-(l-1)) - \beta(\alpha; l, n-l))$$
$$= \sum_{l=2}^{r} \beta(\alpha; l-1, n-(l-1)) -$$
$$\sum_{l=1}^{r} \beta(\alpha; l, n-l)$$
$$= \sum_{l=1}^{r-1} \beta(\alpha; l, n-l) - \sum_{l=1}^{r} \beta(\alpha; l, n-l)$$
$$= -\beta(\alpha; r, n-r).$$

This gives the first row of the right-hand side of Equation (40). The last row follows from combining $\frac{1}{n} \sum_{l=1}^{n} \beta'(\alpha; l, n-l+1) = \frac{1}{n} \sum_{l=1}^{n-1} \beta'(\alpha; l, n-l+1) + \frac{1}{n}\beta'(\alpha; n, 1)$, with the first row of Equation (40) with $r = n-1$, and the last row of Equation (41). ∎

APPENDIX D
PROOF OF THEOREM 2

Proof: We only prove the individual case in Equation (20). The global case follows by averaging both sides of Equation (20) over the probe identity population.

We have to prove for $\int_{0}^{1} \rho(\alpha|\omega)\beta(\alpha; r, n-r)d\alpha$ in Equation (16) that $\int_{0}^{1} \rho(\alpha|\omega)\beta(\alpha; r, n-r)d\alpha = \rho(\frac{r}{n}|\omega) + O(\frac{1}{n})$ for $1 \leq r < n$. By applying Taylor's Theorem with the Lagrange form of the remainder term [34] we as an approximation of $\rho(\alpha|\omega)$ around $\frac{r}{n}$

$$\rho(\alpha|\omega) = \rho\left(\frac{r}{n}|\omega\right) + \rho'\left(\frac{r}{n}|\omega\right)\left(\alpha - \frac{r}{n}\right)$$
$$+ \frac{\rho''(\xi|\omega)}{2}\left(\alpha - \frac{r}{n}\right)^2, \tag{42}$$

with $0 \leq \xi \leq 1$. Note that ξ depends on α. On substitution of Equation (42) into $\int_0^1 \rho(\alpha|\omega)\beta(\alpha; r, n-r)\mathrm{d}\alpha$, the first term of the right-hand side of Equation (42) remains unchanged, because it is a constant. The second vanishes because $\mathrm{E}\{\alpha\} = \frac{r}{n}$, cf. Equation (18), and the remainder term cannot be computed analytically, but with Equation (19) we have

$$\left| \int_0^1 \frac{\rho''(\xi|\omega)}{2}\left(\alpha - \frac{r}{n}\right)^2 \beta(\alpha; k, n)\mathrm{d}\alpha \right|$$

$$\leq \max_\xi \left| \frac{\rho''(\xi|\omega)}{2} \right| \int_0^1 \left(\alpha - \frac{r}{n}\right)^2 \beta(\alpha; k, n)\mathrm{d}\alpha$$

$$= \max_\xi \left| \frac{\rho''(\xi|\omega)}{2} \right| \frac{1}{n+1}\left(\frac{r}{n}\right)\left(1 - \frac{r}{n}\right)$$

$$= \mathrm{O}\left(\frac{1}{n}\right). \tag{43}$$

This completes the proof. ∎

APPENDIX E
PROOF OF COROLLARY 2

Proof: We will only prove the individual case in Equation (24). The global case follows by averaging both sides of Equation (24) over the probe population. Starting from Equation (16) we find that

$$\frac{1}{n}\sum_{r=1}^n \mathrm{cmc}(r|\omega; n)$$

$$= \int_0^1 \rho(\alpha|\omega)\left(\frac{1}{n}\sum_{r=1}^{n-1}\beta(\alpha; r, n-r)\right)\mathrm{d}\alpha + \frac{1}{n}.$$

Corollary 2 holds if $\sum_{r=1}^{n-1}\beta(\alpha; r, n-r) = n - 1$. Using the definition Equation (15) and the well-known relation

$$(a+b)^m = \sum_{l=0}^m \frac{m!}{l!(m-l)!}a^l b^{m-l}$$

with $a = \alpha$ and $b = 1 - \alpha$ and $m = n - 2$, we write

$$\sum_{r=1}^{n-1}\beta(\alpha; r, n-r)$$

$$= \sum_{r=1}^{n-1}\frac{(n-1)!}{(r-1)!(n-r-1)!}\alpha^{r-1}(1-\alpha)^{n-r-1}$$

$$= \sum_{l=0}^{n-2}\frac{(n-1)!}{l!(n-2-l)!}\alpha^l(1-\alpha)^{n-2-l}$$

$$= (n-1)\sum_{l=0}^{n-2}\frac{(n-2)!}{l!(n-2-l)!}\alpha^l(1-\alpha)^{n-2-l}$$

$$= n - 1,$$

which completes the proof of Equation (24). ∎

REFERENCES

[1] J. Sanchez del Rio, D. Moctezuma, C. Conde, I. M. de Diego, and E. Cabello, "Automated border control e-gates and facial recognition systems," *Comput. Secur.*, vol. 62, pp. 49–72, Sep. 2016.

[2] D. Broeders, "The new digital borders of europe: Eu databases and the surveillance of irregular migrants," *Int. Sociol.*, vol. 22, no. 1, pp. 71–92, 2007.

[3] P. Grother, M. Ngan, and G. Quinn, "NISTIR 8173: Face in video evaluation (FIVE) face recognition of non-cooperative subjects," Nat. Inst. Stand. Technol., Gaithersburg, MD, USA, Rep. 8173, Mar. 2017.

[4] A. Y. Boumedine, S. Bentaieb, and A. Ouamri, "An improved KNN classifier for 3D face recognition based on SURF descriptors," *J. Appl. Security Res.*, to be published.

[5] H. Luo, S. Cen, Q. Ding, and X. Chen, "Frontal face reconstruction based on detail identification, variable scale self-attention and flexible skip connection," *Neural Comput. Appl.*, vol. 34, pp. 10561–10573, Jul. 2022.

[6] Q. Zhu, Z. Mu, and L. Yuan, "Corresponding keypoint constrained sparse representation three-dimensional ear recognition via one sample per person," *IET Biometr.*, vol. 11, no. 3, pp. 225–248, 2022.

[7] J. Chen, Z. Wang, C. Zheng, K. Zeng, Q. Zou, and Z. Xiong, "Understanding dynamic associations: Gait recognition via cross-view spatiotemporal aggregation network," *IEEE Trans. Circuits Syst. Video Technol.*, early access, Jun. 23, 2022, doi: 10.1109/TCSVT.2022.3185642.

[8] P. J. Phillips et al., "NISTIR 6965: Face recognition vendor test 2002: Evaluation report," Nat. Inst. Stand. Technol., Gaithersburg, MD, USA, Rep. 6965, Mar. 2007.

[9] P. Grother and P. J. Phillips, "Models of large population recognition performance," in *Proc. IEEE Comput. Soc. Conf. Comput. Vis. Pattern Recognit.*, Jun. 2004, pp. 68–75.

[10] R. Bolle, J. Connel, S. Pankanti, N. Ratha, and A. Senior, "The relation between the ROC curve and the CMC," in *Proc. 4th IEEE Workshop Autom. Identif. Adv. Technol.*, 2005, pp. 15–20.

[11] D.O. Gorodnichy, "Multi-order analysis framework for comprehensive biometric performance evaluation," in *SPIE Conference on Defense, Security and Sensing*, volume 7667 76670G of *Proc. DS108: Biometr. Technol. Human Identificat. VII*, 2010, pp. 1–12.

[12] D.O. Gorodnichy, "Multi-order score analysis framework and its application to designing and evaluating biometric systems," in *Proc. IEEE Workshop Comput. Intell. Biometr. Identity Manag. (CIBIM)*, 2011, pp. 44–53.

[13] B. DeCann and A. Ross, "Can a "poor" verification system be a "good" identification system?" in *Proc. IEEE Workshop Inf. Foren. Secur. (WIFS)*, vol. 1, 2012, pp. 31–36.

[14] B. DeCann and A. Ross, "Relating ROC and CMC curves via the biometric menagerie," in *Proc. Biometr. Theory Appl. Syst. (BTAS)*, 2013, pp. 1–8.

[15] "Information technology–Vocabulary–Part 37: Biometrics, ISO/IEC Standard 2382–37, 2022.

[16] N. Mansfield and J. L. Wayman, "U.K. biometric working group best practice document," Nat. Phys. Lab., Teddington, U.K., Rep. CMSC 14/02, 2002.

[17] P. J. Phillips et al., "Overview of the face recognition grand challenge," in *Proc. IEEE Conf. Computer Vis. Pattern Recognit.*, vol. 1. 2005, pp. 947–954.

[18] R. Cappelli, M. Ferrara, A. Franco, and D. Maltoni, "Fingerprint verification competition 2006," *Biometr. Technol. Today*, vol. 15, no. 7, pp. 7–9, 2007.

[19] N. P. Ramaiah and A. Kumar, "Towards more accurate iris recognition using cross-spectral matching," *IEEE Trans. Image Process.*, vol. 26, no. 1, pp. 208–221, Jan. 2017.

[20] S. Tulyakov and V. Govindaraju, *Predicting Performance in Large-Scale Identification Systems by Score Resampling*. Buffalo, NY, USA: Univ. Buffalo, 2011, pp. 363–388.

[21] G. Doddington, W. Liggett, A. Martin, M. Przybocki, and D. Reynolds., "Sheep, goats, lambs and wolves a statistical analysis of speaker performance in the nist 1998 speaker recognition evaluation," in *Proc. Int. Conf. Spoken Lang. Process.*, 1998, pp. 1351–1354.

[22] T. Fawcett, "An introduction to ROC analysis," *Pattern Recognit. Lett.*, vol. 27, no. 8, pp. 861–874, 2006.

[23] C. M. Bishop, *Pattern Recognition and Machine Learning* (Information Science and Statistics). New York, NY, USA: Springer, 2006.

[24] G. H. Hardy and E. M. Wright, *An Introduction to the Theory of Numbers*. Oxford, U.K.: Clarendon Press, 1979.

[25] D. Green and J. Swets, *Signal Detection Theory and Psychophysics*. New York, NY, USA: Wiley, 1966.

[26] T. Fawcett, "ROC graphs: Notes and practical considerations for data mining researchers," HP Lab., Palo Alto, CA, USA, Rep. HPL-2003–4, 2003.

[27] A. M. Bazen and R. N. J. Veldhuis, "Likelihood-ratio-based biometric verification," *IEEE Trans. Circuits Syst. Video Technol.*, vol. 14, no. 1, pp. 86–94, Jan. 2004.

[28] J. Deng, J. Guo, N. Xue, and S. Zafeiriou, "ArcFace: Additive angular margin loss for deep face recognition," in *Proc. IEEE Conf. Comput. Vis. Pattern Recognit.*, 2019, pp. 4690–4699.

[29] P. Viola and M. J. Jones, "Robust real-time face detection," *Int. J. Comput. Vis.*, vol. 57, no. 2, pp. 137–154, 2004.

[30] F. Boutros, N. Damer, F. Kirchbuchner, and A. Kuijper, "Elasticface: Elastic margin loss for deep face recognition," 2021, *arXiv:abs/2109.09416*.

[31] K. Ko, "User's guide to nist biometric image software (NBIS)," Nat. Inst. Stand. Technol., Gaithersburg, MD, USA, Rep. NISTIR 7392, 2007.

[32] John Daugman, "New methods in iris recognition," *IEEE Trans. Syst., Man, Cybern. B, Cybern.*, vol. 37, no. 5, pp. 1167–1175, Oct. 2007.

[33] K. Raja, R. Raghavendra, V. K. Vemuri, and C. Busch, "Smartphone based visible iris recognition using deep sparse filtering," *Pattern Recognit. Lett.*, vol. 57, pp. 33–42, May 2015.

[34] M. Abramowitz and I. A. Stegun, Eds., *Handbook of Mathematical Functions With Formulas, Graphs, and Mathematical Tables*. New York, NY, USA: Dover, 1972.

Raymond N. J. Veldhuis (Senior Member, IEEE) graduated from the University of Twente, The Netherlands, in 1981. He received the Ph.D. degree from Nijmegen University in 1988 on a thesis entitled Adaptive Restoration of Lost Samples in Discrete-Time Signals and Digital Images. From 1982 to 1992, he was a Researcher with Philips Research Laboratories, Eindhoven, in various areas of digital signal processing. From 1992 to 2001, he was involved in the field of speech processing. He is currently a part-time Professor with the University of Twente, Enschede, The Netherlands, and NTNU, Gjøvik, Norway. His main research topic is machine learning for biometrics, with a focus on face recognition and biometric template protection. The research is both applied and fundamental.

Kiran Raja (Senior Member, IEEE) received the Ph.D. degree in computer science from the Norwegian University of Science and Technology, Norway, in 2016, where he is a Faculty Member with the Department of Computer Science. His main research interests include statistical pattern recognition, image processing, and machine learning with applications to biometrics, security, and privacy protection. He was participating in EU projects SOTAMD, iMARS, and other national projects. He is a member of European Association of Biometrics (EAB) and the Chair of Academic Special Interest Group at EAB. He serves as a reviewer for number of journals and conferences. He is also a member of the editorial board for various journals.